Full-potential nonorthogonal local-orbital minimum-basis band-structure scheme

Klaus Koepernik
MPI ''Physics of Complex Systems,'' D–01887 Dresden, Germany

Helmut Eschrig
IFW Dresden, P.O. Box 270016, D-01171, Dresden, Germany
(Received 16 March 1998; revised manuscript received 29 July 1998)

We present a full-potential band-structure scheme based on the linear combination of overlapping nonorthogonal orbitals. The crystal potential and density are represented as a lattice sum of local overlapping nonspherical contributions. The decomposition of the exchange and correlation potential into local parts is done using a technique of partitioning of unity resulting in local shape functions, which add exactly to unity in the whole crystal and which are very easily treated numerically. The method is all-electron, which means that core relaxation is properly taken into account. Nevertheless, the eigenvalue problem is reduced to the dimension of a minimum valence orbital basis only. Calculations on *sp* and transition metals give results comparable to other full-potential methods. The calculations on the diamond lattice demonstrate the applicability of our approach to open structures. The consequent local description of all real-space functions allows the treatment of substitutional disordered materials. [S0163-1829(99)09303-0]

I. INTRODUCTION

During the past few decades enormous progress has been made in the computation of the solid state using density-functional theory (DFT) within the framework of the Kohn-Sham theory. It was enabled by the development of a number of self-consistent band-structure schemes such as, e.g., the Korringa-Kohn-Rostocker (KKR) method,[1] the augmented spherical waves (ASW) method,[2] the linear augmented-plane-waves (LAPW) method,[3] and the linear muffin-tin orbitals (LMTO) method.[3] Due to the limited performance of former computer facilities, the earlier methods were based on some approximations allowing rather realistic calculations with moderate numerical effort. A common feature of all those approaches is an approximate representation of the crystal potential. The crystal is subdivided into atomic spheres wherein a spherical potential is calculated and an interstitial region has a constant potential [muffin-tin (MT) or atomic-sphere approximation (ASA)]. Although this was a rather inexact approximation, the results obtained were quite reasonable at least for close-packed structures. For open structures additional empty spheres were introduced.

Later on, these methods were further improved by taking into account the real potential shape within the whole crystal. For most band structure methods there exist full-potential versions [FPLAPW,[4,5] FPKKR,[6] FPLMTO,[7] and FPASW (Ref. 8)]. Meanwhile, Gaussian basis sets as used in quantum chemistry have been successfully applied to the single-electron Kohn-Sham problem.[9,10] With increasing computer power these accurate methods became more and more important since many substances of interest have complex structures and exhibit complex physical behavior which is rather sensitive to the approximations made during the calculations. Gradient corrections to the widely used local-spin-density approximation (LSDA) demand a precise density and potential representation. The crystal-field effects in $4f$ systems are strongly dependent on the quality of the determined potential. The magnetic properties of some materials are quite complex, including noncollinear spin alignment and very small energy differences between different spin configurations. As was shown, for instance, in Ref. 11 and as will be seen in Sec. IV C of this paper, the magnetic moments are sensitive to the potential approximations made.

Besides the above-mentioned band-structure schemes related to the ASA or MT construction, other approaches exist that use a different potential representation. There are, for instance, the pseudopotential methods[12–14] which to a certain degree are full-potential by construction.

Another approach was followed by the linear-combination of atomic orbitals (LCAO) scheme.[15,16] In Ref. 15, the crystal potential is represented by a sum of overlapping local spherical contributions. On the one hand, this construction yields some nonsphericity within the atomic volume and, on the other hand, it provides a nontrivial potential shape in the interstitial region. It turned out that the LCAO method gives rather good results for open structures (e.g., intercalates[17]) and for crystal-field calculations.[18] Furthermore, the numerical effort of this method is moderate, which enables the treatment of rather large unit cells.

An application of the DFT to substitutionally disordered materials is possible by including the coherent potential approximation (CPA) into the band-structure schemes in a charge self-consistent manner. Such CPA versions exist for the KKR and LMTO methods.[19,20] By its very nature, the CPA needs a treatment of the electronic structure in terms of local ingredients. Therefore, tight-binding (TB) variants of KKR (Ref. 21) and LMTO (Ref. 22) have been designed.

Recently, an LCAO-CPA (Ref. 23) was developed which combines the advantage of the local formulation (necessary for a description of substitutional disorder) with a good potential representation. The underlying generalized Blackman-Esterling-Berk (BEB) CPA is well-suited to treat partial disorder. Substitutional disorder at a site is in a certain sense a local effect. If any CPA theory is used to describe a disor-

dered material, a mechanism of distinguishing the influence of the local occupancy on the potential and wave function is needed. Since plane waves are extended over the whole crystal, their usefulness in CPA schemes is limited.

Projection on local orbitals is needed for many other purposes, for instance to extract model parameters from band-structure calculations or to interpret the results in chemical terms. Chemical bonding can be analyzed using the concept of crystal orbital overlap population (COOP).[24] Projection on local orbitals is never free from ambiguity in the choice of those orbitals. Our approach has the advantage that it finds the best local orbitals of a minimum basis with respect to total energy minimization.

The present work describes a new full-potential nonorthogonal local-orbital minimum basis band-structure scheme (FPLO). It is based on the construction of the extended crystal wave functions via a linear combination of overlapping nonorthogonal basis orbitals. The representation of the density and potential is again as a lattice sum of local overlapping contributions. But these contributions now exhibit nonsphericity via an angular momentum expansion. Thus, the total lattice sum of these local functions converges in a controlled manner to the real crystal density/potential with increasing angular momentum cutoff. The core electrons are treated in the same manner as the valence electrons, which results in an all-electron band-structure scheme. Nevertheless, an algebraic transformation based on the fact that core orbitals from different sites do not overlap reduces the calculational effort considerably.

The use of local functions in real space is an important presumption for the incorporation of the generalized BEB-CPA. The method presented here therefore applies directly to our recent work.[23] To achieve this local decomposition we introduce the tool of partitioning of unity, resulting in shape functions, which to the best of our knowledge were not used before in this form (Sec. II F). The shape functions are strictly local, and their lattice sum gives exactly unity in the whole crystal. These functions are smooth and may easily be calculated without sacrificing computer time. Other approaches to build shape functions were used by Becke[25] and by Stefanou *et al.*[26] Related to the shape functions are the fitting functions used in the linear combination of Gaussian-type orbitals-fitting function technique (LCGTO-FF), see, e.g., Refs. 10,27,28. The approach of Becke shows some parallels to our construction, however the unity condition is achieved in different ways. Our method assures this condition from the beginning by definition, while Becke uses a normalization procedure to finally obtain the right shape functions. In our opinion, this latter procedure is not well-suited for the application to extended solids and is much more time consuming than the method proposed here.

Due to the restriction to a minimum basis, the computational effort is rather limited and comparable to MT or ASA approximations. Nevertheless, lattice parameters, bulk moduli, and magnetic moments coincide very well with FPLAPW results, and total energies per atom are systematically a few mHartree above the FPLAPW values.

The paper is organized as follows. In Sec. II the concepts for the solution of the Kohn-Sham equation and the recalculation of the crystal density and potential are explained. Sections II C and II F are dedicated to the special tool of partitioning of unity, resulting in two different kinds of shape functions used to decompose the overlap density and the exchange and correlation potential into local contributions. Details of the actual numerical implementation are discussed in Sec. III. Finally, in Sec. IV we apply the scheme to typical examples to compare calculated lattice constants, bulk moduli, magnetic moments, and total energies with other band structure methods and with experiment.

II. THE METHODS

Our approach is based on the density-functional theory within the framework of the Kohn-Sham algorithm. This task splits into two parts: solution of the Kohn-Sham equation and treatment of real space functions such as density and potential, including the solution of Poisson's equation. While the Kohn-Sham problem for a given potential may be solved in various ways with sufficient accuracy, the recalculation of the true density and the potential requires more skill. An important point in going beyond approximate schemes based on cellular decompositions is to construct both the Kohn-Sham wave functions and the density/potential by similar means, trying to avoid expensive transformations between different numerical representations. This work uses a linear combination of overlapping local orbitals to construct the Kohn-Sham solutions. This implies the use of localized overlapping potential contributions to represent the crystal potential. Above all, we will avoid the use of Fourier series, because matrix elements between local orbitals and the Fourier transformed potential are time consuming.

The method will be formulated completely within a local language aiming at rather accurate but fast calculations. Hence, the LCAO-CPA can be incorporated directly within this scheme. Since the disorder theory was described in detail elsewhere, here we will concentrate on the ordered crystal only.

A. Nonorthogonal local-orbital basis

Denote a regular lattice by $\mathbf{R}+\mathbf{s}$, where $\mathbf{R}$ is a Bravais vector and $\mathbf{s}$ is a basis vector of the unit cell. For the crystal potential we use the decomposition

$$v(\mathbf{r}) = \sum_{\mathbf{R}+\mathbf{s},L} v_{\mathbf{s},L}(|\mathbf{r}-\mathbf{R}-\mathbf{s}|) Y_L(\mathbf{r}-\mathbf{R}-\mathbf{s}) \qquad (1)$$

with Y_L being the real spherical harmonics. The sum over $L=lm$ should converge under circumstances which will be elucidated below, and thus we approximate the crystal potential using a cutoff $L_{\max}$. The definition of the local potentials $v_{\mathbf{s},L}$ follows later.

To solve the Kohn-Sham equations we need a representation of the extended crystal states, here chosen to be a nonorthogonal local-orbital representation. This has several advantages as we will see. One point was already mentioned above, the applicability to the generalized local-orbital coherent-potential theory (FPLO-CPA).

The extended states are expanded in terms of localized atomiclike basis orbitals

$$\langle \mathbf{r}|\mathbf{R}\mathbf{s}L\rangle = \phi^l_{\mathbf{s}}(|\mathbf{r}-\mathbf{R}-\mathbf{s}|) Y_L(\mathbf{r}-\mathbf{R}-\mathbf{s}). \qquad (2)$$

Several orbitals with the same angular momentum L are permitted. In all that follows we understand a principal quantum number or/and a spin quantum number as absorbed into the subscript L. The basis orbitals are taken to be solutions of a Schrödinger equation with a single spherical potential chosen to consist of two parts:

$$v^{\mathrm{at}}(r)=\frac{1}{4\pi}\int v(\mathbf{r}-\mathbf{R}-\mathbf{s})d\Omega \quad +v^{\mathrm{conf}}. \tag{3}$$

The first part is the spherically averaged crystal potential, while the second is the confining potential

$$v^{\mathrm{conf}}=\left(\frac{r}{r_0}\right)^4 \tag{4}$$

discussed extensively elsewhere.[15,23] Its radius parameter r_0 has been shown in Ref. 15 to scale basically with the 3/2 power of the lattice constant, and hence we represent it as

$$r_0=\left(\frac{x_0 r_{\mathrm{NN}}}{2}\right)^{3/2}, \tag{5}$$

where r_{NN} is the nearest-neighbor distance and the new parameter x_0 is roughly independent of lattice spacing.

The confining potential serves to compress the local valence basis orbitals. Those compressed orbitals have higher energy levels and are more suitable for the construction of extended wave functions compared to their uncompressed counterparts. The confining potential is applied to the valence states, which are distinguished from core orbitals by the definition that they are all orbitals not overlapping from different sites. The overlapping orbitals are the valence orbitals. The overlap between core and valence orbitals from different sites may of course be nonzero.

The extended state labeled by crystal momentum $\mathbf{k}$ and band index n is constructed as a linear combinations of Bloch sums:

$$|\mathbf{k}n\rangle=\sum_{\mathbf{R}\mathbf{s}L}|\mathbf{R}\mathbf{s}L\rangle c_{L\mathbf{s}}^{\mathbf{k}n}e^{i\mathbf{k}(\mathbf{R}+\mathbf{s})} \quad . \tag{6}$$

Here, no distinction between core and valence orbitals is made. Inserting this ansatz into the Kohn-Sham equation

$$H|\mathbf{k}n\rangle=|\mathbf{k}n\rangle\varepsilon_{\mathbf{k}n} \tag{7}$$

yields

$$\sum_{\mathbf{R}\mathbf{s}L}[\langle\mathbf{0}\mathbf{s}'L'|H|\mathbf{R}\mathbf{s}L\rangle-\langle\mathbf{0}\mathbf{s}'L'|\mathbf{R}\mathbf{s}L\rangle\varepsilon^{\mathbf{k}n}]c_{L\mathbf{s}}^{\mathbf{k}n}e^{i\mathbf{k}(\mathbf{R}+\mathbf{s}-\mathbf{s}')}=0. \tag{8}$$

The Hamiltonian and overlap matrices read

$$H_{\mathbf{0}\mathbf{s}'\mathbf{R}\mathbf{s}}^{L'L}=\langle\mathbf{0}\mathbf{s}'L'|H|\mathbf{R}\mathbf{s}L\rangle, \tag{9}$$

$$S_{\mathbf{0}\mathbf{s}'\mathbf{R}\mathbf{s}}^{L'L}=\langle\mathbf{0}\mathbf{s}'L'|\mathbf{R}\mathbf{s}L\rangle. \tag{10}$$

These matrix elements are further simplified by the core-valence distinction. By definition, core orbitals $|\mathbf{R}\mathbf{s}c\rangle$ obey

$$\langle\mathbf{R}'\mathbf{s}'c'|\mathbf{R}\mathbf{s}c\rangle=\delta_{c'c}\delta_{\mathbf{R}'+\mathbf{s}',\mathbf{R}+\mathbf{s}}, \tag{11}$$

$$H|\mathbf{R}\mathbf{s}c\rangle=|\mathbf{R}\mathbf{s}c\rangle\varepsilon_{\mathbf{s}c}. \tag{12}$$

A core orbital is so strongly localized that it does not noticeably deform due to the difference between the true crystal potential $v(\mathbf{r})$ of Eq. (1) and its spherical average around the orbital center. Basis orbitals for which this is not true are treated as valence orbitals. It is clear that in this way the classification of orbitals as core or valence is dictated by accuracy demands. (For example, $3s$ and $3p$ orbitals of $3d$ metals are often treated as valence orbitals.)

Further on, we use subscripts c for core orbitals and v for valence orbitals. If the distinction is not important, we use L. Due to Eq. (11), the overlap matrix now contains four blocks:

$$S=\begin{pmatrix}S_{cc} & S_{cv}\\ S_{vc} & S_{vv}\end{pmatrix} \tag{13}$$

with

$$S_{cc}=\langle\mathbf{R}'\mathbf{s}'c'|\mathbf{R}\mathbf{s}c\rangle=\delta_{c'c}\delta_{\mathbf{R}'+\mathbf{s}',\mathbf{R}+\mathbf{s}},$$

$$S_{cv}=\langle\mathbf{R}'\mathbf{s}'c'|\mathbf{R}\mathbf{s}v\rangle,$$

$$S_{vc}=\langle\mathbf{R}'\mathbf{s}'v'|\mathbf{R}\mathbf{s}c\rangle=S_{cv}^{\dagger},$$

$$S_{vv}=\langle\mathbf{R}'\mathbf{s}'v'|\mathbf{R}\mathbf{s}v\rangle.$$

The Hamiltonian matrix simplifies to

$$H=\begin{pmatrix}H_{cc} & H_{cc}S_{cv}\\ S_{vc}H_{cc} & H_{vv}\end{pmatrix} \tag{14}$$

with

$$H_{cc}=\langle\mathbf{R}'\mathbf{s}'c'|H|\mathbf{R}\mathbf{s}c\rangle=\varepsilon_{\mathbf{s}c}\delta_{c'c}\delta_{\mathbf{R}'+\mathbf{s}',\mathbf{R}+\mathbf{s}},$$

$$H_{vv}=\langle\mathbf{R}'\mathbf{s}'v'|H|\mathbf{R}\mathbf{s}v\rangle.$$

(As a slight generalization to crystal-field-split core levels, $H_{cc}=\varepsilon_{\mathbf{s}c'c}\delta_{\mathbf{R}'+\mathbf{s}',\mathbf{R}+\mathbf{s}}$ would pose no problems.) The actual core-valence and valence-valence matrix elements consist of one-center and multicenter integrals. The on-site elements are

$$\langle\mathbf{s}L'|H|\mathbf{s}L\rangle=\langle\mathbf{s}L'|-\frac{\Delta}{2}+\sum_{L_1}v_{\mathbf{s}L_1}(|\mathbf{r}-\mathbf{s}|)Y_{L_1}(\mathbf{r}-\mathbf{s})|\mathbf{s}L\rangle+\langle\mathbf{s}L'|\sum_{\substack{\mathbf{R}'+\mathbf{s}'(\neq\mathbf{s})\\ L_1}}v_{\mathbf{s}'L_1}(|\mathbf{r}-\mathbf{R}'-\mathbf{s}'|)Y_{L_1}(\mathbf{r}-\mathbf{R}'-\mathbf{s}')|\mathbf{s}L\rangle \quad . \tag{15}$$

Here the second expression contains the off-site part of the crystal field contribution to the potential at $\mathbf{s}$, which is a two-center term. The off-site elements for $\mathbf{s}'\neq\mathbf{R}+\mathbf{s}$ are

$$\langle \mathbf{s}'L'|H|\mathbf{R}\mathbf{s}L\rangle = \langle \mathbf{s}'L'|-\frac{\Delta}{2}+\sum_{L_1} v_{\mathbf{s}'L_1}(|\mathbf{r}-\mathbf{s}'|)Y_{L_1}(\mathbf{r}-\mathbf{s}')+\sum_{L_2} v_{\mathbf{s}L_2}(|\mathbf{r}-\mathbf{R}-\mathbf{s}|)Y_{L_2}(\mathbf{r}-\mathbf{R}-\mathbf{s})|\mathbf{R}\mathbf{s}L\rangle$$

$$+\langle \mathbf{s}'L'| \sum_{\substack{(\mathbf{s}'\neq)\mathbf{R}''+\mathbf{s}''(\neq\mathbf{R}+\mathbf{s}) \\ L_1}} v_{\mathbf{s}''L_1}(|\mathbf{r}-\mathbf{R}''-\mathbf{s}''|)Y_{L_1}(\mathbf{r}-\mathbf{R}''-\mathbf{s}'')|\mathbf{R}\mathbf{s}L\rangle \quad , \tag{16}$$

where in the first line each integral is a two-center term. The last line, the three-center terms, are unavoidable in our representation, but due to the compression of local functions they are rather limited in number and are possible to calculate in moderate computer time. Details of the numerics are in Sec. III.

Now, we introduce an algebraic transformation[29] to reduce the dimension of the problem using the special form of the Hamiltonian Eq. (14) and the overlap matrix Eq. (13). It applies to both lattice site and Bloch state representations. Since the core-core block of S is the unit matrix, we may perform a simplified Cholesky decomposition of S

$$S = S^l S^r = \begin{pmatrix} 1 & 0 \\ S^l_{vc} & S^l_{vv} \end{pmatrix}\begin{pmatrix} 1 & S^r_{cv} \\ 0 & S^r_{vv} \end{pmatrix} \tag{17}$$

implying the following relations:

$$S_{vc} = S^l_{vc} = S^{r\dagger}_{cv} = S^\dagger_{cv}, \quad S^l_{vv}S^r_{vv} = S_{vv} - S_{vc}S_{cv}. \tag{18}$$

For later use in the secular equation, the inverse of this Cholesky decomposition is

$$S^{l-1} = \begin{pmatrix} 1 & 0 \\ -S^{l-1}_{vv}S_{vc} & S^{l-1}_{vv} \end{pmatrix}, \quad S^{r-1} = \begin{pmatrix} 1 & -S_{cv}S^{r-1}_{vv} \\ 0 & S^{r-1}_{vv} \end{pmatrix}. \tag{19}$$

The matrix equation (8) reads

$$HC = SCE, \tag{20}$$

where C has matrix elements $c_{L\mathbf{s},n}(\mathbf{k})$ and $E = \mathrm{diag}(\varepsilon_{\mathbf{k}n})$. This can be rewritten as

$$S^{l-1}HS^{r-1}D = DE, \quad D = S^rC, \tag{21}$$

where D is the unitary matrix diagonalizing $S^{l-1}HS^{r-1}$. Since the c-c block of this latter matrix is already diagonal,

$$D_{cc} = 1. \tag{22}$$

Moreover, the c-v block of $S^{l-1}HS^{r-1}$ vanishes as is easily seen from Eqs. (14) and (19), hence $D_{cv}=0$ (even if H_{cc} were not diagonal, in which case only $D_{cc}\neq 1$), and we are left with the reduced eigenvalue problem

$$S^{l-1}_{vv}(H - S_{vc}H_{cc}S_{cv})S^{r-1}_{vv}D_{vv} = D_{vv}E_v, \tag{23}$$

with an ordinary pseudo-Hamiltonian in parentheses. Finally, the wave-function coefficient matrix C is obtained as

$$C = S^{r-1}D = \begin{pmatrix} 1 & -S_{cv}S^{r-1}_{vv}D_{vv} \\ 0 & S^{r-1}_{vv}D_{vv} \end{pmatrix}. \tag{24}$$

Thus we have solved the eigenvalue problem Eq. (8) by effectively solving a much smaller problem Eq. (23), since, at least for heavy atoms, the number of core orbitals exceeds the number of valence orbitals considerably.

B. The electron density

Next the density must be recalculated. The local orbital representation is

$$n = \sum_{\mathbf{k}n}^{\mathrm{occ}} |\mathbf{k}n\rangle\langle\mathbf{k}n| \tag{25}$$

$$= \sum_{\mathbf{k}n}^{\mathrm{occ}} \sum_{\substack{\mathbf{R}\mathbf{s}L \\ \mathbf{R}'\mathbf{s}'L'}} |\mathbf{R}\mathbf{s}L\rangle c^{\mathbf{k}n}_{\mathbf{s}L} e^{i\mathbf{k}(\mathbf{R}+\mathbf{s}-\mathbf{R}'-\mathbf{s}')} c^{\dagger\mathbf{k}n}_{\mathbf{s}'L'}\langle\mathbf{R}'\mathbf{s}'L'|. \tag{26}$$

This expression may be separated into on-site and off-site terms. Both classes again are split into core-core, core-valence, and valence-valence contributions. The core-core density has only on-site terms and simplifies to

$$n^{cc} = \sum_{\mathbf{R}\mathbf{s}} n^{\mathrm{net},cc}_{\mathbf{R}\mathbf{s}}, \tag{27}$$

$$n^{\mathrm{net},cc}_{\mathbf{R}\mathbf{s}} = \sum_c |\mathbf{R}\mathbf{s}c\rangle\langle\mathbf{R}\mathbf{s}c| + \sum_{\mathbf{k}n}^{\mathrm{occ}} \sum_{cc'} |\mathbf{R}\mathbf{s}c\rangle c^{\mathbf{k}n}_{\mathbf{s}c} c^{\dagger\mathbf{k}n}_{\mathbf{s}c'}\langle\mathbf{R}\mathbf{s}c'|. \tag{28}$$

The first term of Eq. (28) is due to the left block column of Eq. (24) and the right term contains the coupling of core orbitals into valence-band states via core-valence orthogonalizations (C_{cv}). Here and further on, the band index n is restricted to valence bands only. The valence-valence on-site term is

$$n^{\mathrm{net},vv}_{\mathbf{R}\mathbf{s}} = \sum_{\substack{\mathbf{k}n \\ vv'}}^{\mathrm{occ}} |\mathbf{R}\mathbf{s}v\rangle c^{\mathbf{k}n}_{\mathbf{s}v} c^{\dagger\mathbf{k}n}_{\mathbf{s}v'}\langle\mathbf{R}\mathbf{s}v'|. \tag{29}$$

Then, again because of nonorthogonality between core and valence orbitals, there is an on-site core-valence contribution

$$n^{\mathrm{net},cv}_{\mathbf{R}\mathbf{s}} = 2\,\mathrm{Re}\sum_{\substack{\mathbf{k}n \\ cv'}}^{\mathrm{occ}} |\mathbf{R}\mathbf{s}c\rangle c^{\mathbf{k}n}_{\mathbf{s}c} c^{\dagger\mathbf{k}n}_{\mathbf{s}v'}\langle\mathbf{R}\mathbf{s}v'|. \tag{30}$$

The on-site or net part of the electron density is the sum of those three contributions,

$$n^{\mathrm{net}}_{\mathbf{R}\mathbf{s}} = n^{\mathrm{net},cc}_{\mathbf{R}\mathbf{s}} + n^{\mathrm{net},vv}_{\mathbf{R}\mathbf{s}} + n^{\mathrm{net},cv}_{\mathbf{R}\mathbf{s}}. \tag{31}$$

Note that the orbitals are well-localized functions which fall off essentially to zero within the nearest-neighbor distance. Furthermore, the maximum angular momentum of the orbitals is $l=3$ for f functions. Thus, the net charge density contains maximum $l=6$ contributions if projected onto a basis of spherical harmonics.

Now consider the off-site terms of the density, the overlap density. The core-valence contribution is

$$n^{\mathrm{ovl},cv}=\sum_{\mathbf{k}n}^{\mathrm{occ}}\sum_{\substack{\mathbf{R}'+\mathbf{s}'\neq\mathbf{R}+\mathbf{s}\\ cv'}}|\mathbf{R}\mathbf{s}c\rangle c_{\mathbf{s}c}^{\mathbf{k}n}e^{i\mathbf{k}(\mathbf{R}+\mathbf{s}-\mathbf{R}'-\mathbf{s}')}c_{\mathbf{s}'v'}^{\dagger\mathbf{k}n}\langle\mathbf{R}'\mathbf{s}'v'|+\sum_{\mathbf{k}n}^{\mathrm{occ}}\sum_{\substack{\mathbf{R}'+\mathbf{s}'\neq\mathbf{R}+\mathbf{s}\\ vc'}}|\mathbf{R}\mathbf{s}v\rangle c_{\mathbf{s}v}^{\mathbf{k}n}e^{i\mathbf{k}(\mathbf{R}+\mathbf{s}-\mathbf{R}'-\mathbf{s}')}c_{\mathbf{s}'c'}^{\dagger\mathbf{k}n}\langle\mathbf{R}'\mathbf{s}'c'| \tag{32}$$

and the valence-valence term reads

$$n^{\mathrm{ovl},vv}=\sum_{\mathbf{k}n}^{\mathrm{occ}}\sum_{\substack{\mathbf{R}'+\mathbf{s}'\neq\mathbf{R}+\mathbf{s}\\ vv'}}|\mathbf{R}\mathbf{s}v\rangle c_{\mathbf{s}v}^{\mathbf{k}n}e^{i\mathbf{k}(\mathbf{R}+\mathbf{s}-\mathbf{R}'-\mathbf{s}')}c_{\mathbf{s}'v'}^{\dagger\mathbf{k}n}\langle\mathbf{R}'\mathbf{s}'v'|. \tag{33}$$

All those terms entering the overlap expressions cannot directly be divided into local contributions, since they are functions having small cusps at both the centers involved and are nonzero mainly in the region lying between the two centers. Here we have to make approximations concerning the treatment of real space functions, as follows.

C. Partitioning of multicenter terms

Our density treatment results in lattice periodic functions with the structure

$$F(\mathbf{r})=\sum_{ij}\langle\mathbf{r}|i\rangle\langle j|\mathbf{r}\rangle, \tag{34}$$

where i and j denote a pair $(i,j)=(\mathbf{R}+\mathbf{s},\mathbf{R}'+\mathbf{s}')$ of lattice sites. Introduce a rescaled difference coordinate

$$x_{ij}=(\mathbf{r}-\mathbf{R}-\mathbf{s})\cdot\mathbf{P},\quad \mathbf{P}=\frac{\mathbf{R}'+\mathbf{s}'-\mathbf{R}-\mathbf{s}}{|\mathbf{R}'+\mathbf{s}'-\mathbf{R}-\mathbf{s}|^2} \tag{35}$$

taking on values 0 and 1 at the sites i and j, respectively. We choose a real function f with the properties

$$\begin{aligned} &f(x)+f(1-x)=1,\\ &f(x)=1\quad\text{for}\quad x\leqslant 0,\\ &f(x)=0\quad\text{for}\quad x\geqslant 1, \end{aligned} \tag{36}$$

and write

$$\langle\mathbf{r}|i\rangle\langle j|\mathbf{r}\rangle=f_{ij}\langle\mathbf{r}|i\rangle\langle j|\mathbf{r}\rangle+\langle\mathbf{r}|i\rangle\langle j|\mathbf{r}\rangle f_{ji}, \tag{37}$$

where

$$f_{ij}\equiv f(x_{ij}). \tag{38}$$

(Note $x_{ij}=1-x_{ji}$.) This yields immediately

$$F(\mathbf{r})=\sum_{ij}2\,\mathrm{Re}f_{ij}\langle\mathbf{r}|i\rangle\langle j|\mathbf{r}\rangle\equiv\sum_{i}F_i(\mathbf{r}). \tag{39}$$

The point is that this function F_i is much more localized around the center i than the original construct $\Sigma_j\langle\mathbf{r}|i\rangle\langle j|\mathbf{r}\rangle$.

As a three-dimensional function, $F_i(\mathbf{r})$ must still yield a sufficiently rapidly converging expansion in spherical harmonics:

$$\begin{aligned} F_i(\mathbf{r})&=\sum_L F_{\mathbf{s}L}(r_i)Y_L(\mathbf{r}_i),\\ F_{\mathbf{s}L}(r_i)&=\int F_i(\mathbf{r})Y_L^*(\mathbf{r}_i)d\Omega_i, \end{aligned} \tag{40}$$

$$\mathbf{r}_i=\mathbf{r}-\mathbf{R}-\mathbf{s}. \tag{41}$$

Suitable choices of f_{ij} for this goal are considered in Sec. II F, Eq. (76) and (77).

D. The potential

Application of this partitioning method to the overlap density gives a local decomposition of the crystal electron density

$$n(\mathbf{r})=\sum_{\mathbf{R}\mathbf{s},L}n_{\mathbf{s},L}(|\mathbf{r}-\mathbf{R}-\mathbf{s}|)Y_L(\mathbf{r}-\mathbf{R}-\mathbf{s}). \tag{42}$$

From this density we first construct the Coulomb potential, that is, the sum of the Coulomb potentials of the electron density and of the nuclear charge. The angular momentum components of the local charge densities give rise to multipole moments

$$Q_{\mathbf{s}L}=\int_0^\infty dr r^{l+2}n_{\mathbf{s}L}(r) \tag{43}$$

which determine the behavior of the Coulomb potential for large distances,

$$v_{\mathbf{s}L}(r)\propto\frac{Q_{\mathbf{s}L}}{r^{l+1}}. \tag{44}$$

The $l=0$ part is partially compensated by the nuclear charge of the atom $Z_{\mathbf{s}}$ which gives a potential

$$v^{Z}_{\mathbf{s}0}(r) = -\sqrt{4\pi}\frac{Z_{\mathbf{s}}}{r}. \tag{45}$$

The excess multipole moments yielding long ranging potential tails should be compensated by Ewald's method first to get converging lattice sums of local potentials and second to get well-localized potential contributions. We introduce the Ewald densities

$$n^{\mathrm{Ew}}_{\mathbf{s}L}(r) = A_{\mathbf{s}L}\frac{p^3}{\sqrt{\pi^3}} r^l e^{-r^2p^2} \tag{46}$$

with excess moments

$$\frac{A_{\mathbf{s}L}}{4\pi} = \begin{cases} \dfrac{Z_{\mathbf{s}}}{\sqrt{4\pi}} - Q_{\mathbf{s}0}, & l=0 \\ -\dfrac{Q_{\mathbf{s}L}}{N_l}, & l\neq 0 \end{cases} \tag{47}$$

and normalization coefficients

$$N_l = \frac{p^3}{\sqrt{\pi^3}}\int_0^\infty dr r^{2l+2} e^{-r^2p^2} \quad . \tag{48}$$

The sum of the local electron densities and the Ewald densities gives the local Hartree potential

$$v^{\mathrm{H}}_{\mathbf{s}L}(r) = \frac{4\pi}{2l+1}\left[\frac{1}{r^{l+1}}\int_0^r dr' r'^{2+l}\tilde{n}_{\mathbf{s}L}(r') + r^l\int_r^\infty dr' r'^{1-l}\tilde{n}_{\mathbf{s}L}(r')\right] \tag{49}$$

with $\tilde{n} = n + n^{\mathrm{Ew}}$. The local Coulomb potentials now read

$$v^{\mathrm{C}}_{\mathbf{s}L}(r) = v^{\mathrm{H}}_{\mathbf{s}L}(r) - \frac{\sqrt{4\pi}Z_{\mathbf{s}}}{r}\,\delta_{0l} \tag{50}$$

which indeed are well-localized functions. The Ewald contributions have to be subtracted again. We Fourier transform the negative Ewald density:

$$n^{\mathrm{Ew}}_{\mathbf{G}} = -\frac{1}{V_{\mathrm{uc}}}\sum_{\mathbf{s}} e^{-i\mathbf{G}\cdot\mathbf{s}}\sum_L A_{\mathbf{s}L} e^{-G^2/4p^2}\left(\frac{g}{2p^2}\right)^l Y_L(\mathbf{G}). \tag{51}$$

This gives a Fourier-transformed Ewald potential via the Poisson equation

$$v^{\mathrm{Ew}}_{\mathbf{G}} = \frac{4\pi}{|\mathbf{G}|^2} n^{\mathrm{Ew}}_{\mathbf{G}}. \tag{52}$$

Our total electrostatic potential reads

$$v(\mathbf{r}) = \sum_{\mathbf{Rs}} v^{\mathrm{C}}_{\mathbf{s}L}(r) Y_L(\mathbf{r}-\mathbf{R}-\mathbf{s}) + \sum_{\mathbf{G}} v^{\mathrm{Ew}}_{\mathbf{G}} e^{i\mathbf{G}\cdot\mathbf{r}}. \tag{53}$$

This form has a major disadvantage. To calculate matrix elements between local orbitals including Fourier-transformed potentials is a tedious task concerning the calculation time. Hence, we define a partitioning of unity in the lattice [Eq. (66) below; details in Sec. II F] and apply it to the Fourier-transformed part of the potential

$$\begin{aligned} v^{\mathrm{Ew}}(\mathbf{r}) &= v^{\mathrm{Ew}}(\mathbf{r})\sum_{\mathbf{R}+\mathbf{s}} f_s(\mathbf{r}-\mathbf{R}-\mathbf{s}) \\ &= \sum_{\mathbf{R}+\mathbf{s}} v^{\mathrm{Ew}}_{\mathbf{s}}(\mathbf{r}-\mathbf{R}-\mathbf{s}), \\ v^{\mathrm{Ew}}_{\mathbf{s}}(\mathbf{r}-\mathbf{R}-\mathbf{s}) &= v^{\mathrm{Ew}}(\mathbf{r}) f_s(\mathbf{r}-\mathbf{R}-\mathbf{s}). \end{aligned} \tag{54}$$

The resulting local potential $v^{\mathrm{Ew}}_{\mathbf{s}}$ is expanded in terms of spherical harmonics. Thus we have achieved the Hartree potential representation in the form Eq. (1).

The exchange and correlation part of the crystal potential remains. In the local-(spin)-density approximation (LSDA) it is

$$v^{\mathrm{xc}}(\mathbf{r}) = v^{\mathrm{xc}}[n(\mathbf{r})], \tag{55}$$

where $v^{\mathrm{xc}}[n]$ is a parametrization of the exchange-correlation potential of the homogeneous electron liquid of density n. This nonlinear dependence on the electron density requires a special treatment again to achieve the form Eq. (1). We apply the same partitioning of unity as for the Fourier-transformed Ewald potential:

$$v^{\mathrm{xc}}(\mathbf{r}) = \sum_{\mathbf{Rs}} v^{\mathrm{xc}}_{\mathbf{s}}(\mathbf{r}-\mathbf{R}-\mathbf{s}) \tag{56}$$

with

$$v^{\mathrm{xc}}_{\mathbf{s}}(\mathbf{r}-\mathbf{R}-\mathbf{s}) = v^{\mathrm{xc}}[n(\mathbf{r})] f_s(\mathbf{r}-\mathbf{R}-\mathbf{s}). \tag{57}$$

The resulting local exchange-correlation potentials are again expanded in terms of spherical harmonics. Needless to say, partitioning of v^{xc} applies generally and not only for the LSDA.

Collecting all terms we have the following local potentials:

$$v^{\mathrm{cry}}_{\mathbf{s}}(\mathbf{r}) = \sum_L [v^{\mathrm{C}}_{\mathbf{s}L}(r) + v^{\mathrm{Ew}}_{\mathbf{s}L}(r) + v^{\mathrm{xc}}_{\mathbf{s}L}(r)] Y_L(\mathbf{r}) \tag{58}$$

whose sum expresses the total Kohn-Sham crystal potential

$$v^{\mathrm{cry}}(\mathbf{r}) = \sum_{\mathbf{Rs}} v^{\mathrm{cry}}_{\mathbf{s}}(\mathbf{r}-\mathbf{R}-\mathbf{s}) \tag{59}$$

and thus we close the self-consistency cycle of the Kohn-Sham theory. The maximum l to be taken into account is determined first of all by accuracy demands. However, the expansion in terms of spherical harmonics is expected to converge sufficiently fast. At least the maximum l should be twice the maximum orbital momentum l^{orb}, since the maximum momentum which couples to the product of two orbitals at the same site is $2l^{\mathrm{orb}}$.

E. The total energy

The DFT total energy is (with $\mathbf{a}=\mathbf{R}+\mathbf{s}$)

$$E[n(\mathbf{r})]=T[n(\mathbf{r})]+\frac{1}{2}\int\int\frac{n(\mathbf{r})n(\mathbf{r}')}{|\mathbf{r}-\mathbf{r}'|}\,d\mathbf{r}d\mathbf{r}'-\int\sum_{\mathbf{a}}\frac{Z_{\mathbf{a}}}{|\mathbf{r}-\mathbf{a}|}\,n(\mathbf{r})d\mathbf{r}+\frac{1}{2}\sum_{\mathbf{a}\neq\mathbf{b}}\frac{Z_{\mathbf{a}}Z_{\mathbf{b}}}{|\mathbf{a}-\mathbf{b}|}+E_{\mathrm{xc}}[n]. \tag{60}$$

(We do not give a normalization factor. Eventually, we will have lattice sums of local terms which give an extensive total energy; dropping one lattice sum gives the total energy per unit cell.) The first term of Eq. (60) is the Kohn-Sham kinetic energy and is represented using the solution of the Kohn-Sham equation,

$$T[n(\mathbf{r})]=\sum_{\mathbf{k}n}^{\mathrm{occ}}\langle\mathbf{k}n|-\frac{\Delta}{2}|\mathbf{k}n\rangle=\sum_{\mathbf{k}n}^{\mathrm{occ}}\varepsilon^{\mathbf{k}n}-\int d\mathbf{r}n(\mathbf{r})v^{\mathrm{cry}}(\mathbf{r}). \tag{61}$$

In this expression, n runs again over core and valence states, with obvious simplifications for core states. The second term, the Hartree energy of the electrons and the third term, the interaction energy with the nuclei, may partially be combined,

$$\frac{1}{2}\int d\mathbf{r}n(\mathbf{r})\left[\int d\mathbf{r}'\frac{n(\mathbf{r}')}{|\mathbf{r}-\mathbf{r}'|}-\sum_{\mathbf{a}}\frac{Z_{\mathbf{a}}}{|\mathbf{r}-\mathbf{a}|}\right]=\frac{1}{2}\int d\mathbf{r}\sum_{\mathbf{b}}n_{\mathbf{b}}(\mathbf{r}-\mathbf{b})\left[\sum_{\mathbf{a}}[v_{\mathbf{a}}^{\mathrm{C}}(\mathbf{r}-\mathbf{a})+v_{\mathbf{a}}^{\mathrm{Ew}}(\mathbf{r}-\mathbf{a})]\right]. \tag{62}$$

The last expression completely fits our potential and density representation in terms of lattice sums of local functions. The remaining part of the electron-nucleus energy will be combined with the fourth term of Eq. (60), the nucleus-nucleus repulsion energy:

$$\begin{aligned}&-\frac{1}{2}\sum_{\mathbf{a}}\int d\mathbf{r}\frac{Z_{\mathbf{a}}}{|\mathbf{r}-\mathbf{a}|}\left[\sum_{\mathbf{b}}n_{\mathbf{b}}(\mathbf{r}-\mathbf{b})-\sum_{\mathbf{b}\neq\mathbf{a}}Z_{\mathbf{b}}\delta(\mathbf{r}-\mathbf{b})\right]\\&=-\frac{1}{2}\sum_{\mathbf{a}}\int\int d\mathbf{r}'d\mathbf{r}\frac{Z_{\mathbf{a}}\delta(\mathbf{r}'-\mathbf{a})}{|\mathbf{r}-\mathbf{r}'|}\left[\sum_{\mathbf{b}}\tilde{n}_{\mathbf{b}}(\mathbf{r}-\mathbf{b})-\sum_{\mathbf{b}\neq\mathbf{a}}Z_{\mathbf{b}}\delta(\mathbf{r}-\mathbf{b})-n^{\mathrm{Ew}}(\mathbf{r})\right]\\&=-\frac{1}{2}\sum_{\mathbf{a}}Z_{\mathbf{a}}\left[\int\frac{\tilde{n}_{\mathbf{a}}(\mathbf{r})}{r}d\mathbf{r}+v_{\mathbf{a}}^{\mathrm{Ew}}(0)+\sum_{\mathbf{b}\neq\mathbf{a}}(v_{\mathbf{b}}^{\mathrm{C}}(\mathbf{a}-\mathbf{b})+v_{\mathbf{b}}^{\mathrm{Ew}}(\mathbf{a}-\mathbf{b}))\right].\end{aligned} \tag{63}$$

The last line again corresponds to our localized representation. Now the last term to be managed is the exchange and correlation energy,

$$E_{\mathrm{xc}}[n]=\int d\mathbf{r}n(\mathbf{r})\varepsilon_{\mathrm{xc}}(n(\mathbf{r})). \tag{64}$$

The xc energy per unit cell may be expressed using the shape functions

$$E_{\mathrm{xc}}^{\mathrm{uc}}[n]=\sum_{\mathbf{s}}\int d\mathbf{r}f_s(\mathbf{r}-\mathbf{s})n(\mathbf{r})\varepsilon_{\mathrm{xc}}(n(\mathbf{r})) \tag{65}$$

which are integrals over localized smooth functions falling off rapidly, due to the properties of f_s.

F. The shape function

Our task is to find a partitioning of unity on a lattice with basis, that is to find a set $\{f_s\}$ of three-dimensional real functions obeying

$$\sum_{\mathbf{R}+\mathbf{s}}f_s(\mathbf{r}-\mathbf{R}-\mathbf{s})\equiv 1. \tag{66}$$

The subscript s labels the N basis vectors $\mathbf{s}$.

We start with the Hessian form of the equations of lattice planes

$$\mathbf{g}\cdot\mathbf{r}=d_n,\quad \mathbf{g}=\frac{\mathbf{G}}{|\mathbf{G}|},\quad d_n=\frac{2\pi}{|\mathbf{G}|}\,n, \tag{67}$$

where $\mathbf{G}$ is a reciprocal-lattice vector and n runs over all (positive and negative) integers. The sublattice planes corresponding to basis vectors are given by

$$\mathbf{g}\cdot\mathbf{r}=d_n+g_s,\quad g_s=\mathbf{g}\cdot\mathbf{s},\quad 0\leqslant g_s\leqslant\frac{2\pi}{|\mathbf{G}|}. \tag{68}$$

Given $\mathbf{G}$, there are N values g_s, for which we find the minimum distance

$$\gamma_{\mathbf{G}}=\min_{s,s'}^{(+)}|g_s-g_{s'}|, \tag{69}$$

excluding zero differences from consideration.

Finally, we find a $\mathbf{G}$ such that $\gamma_{\mathbf{G}}$ is maximum:

$$\gamma=\max_{\mathbf{G}}\gamma_{\mathbf{G}}=\gamma_{\mathbf{G}_{\max}}. \tag{70}$$

For what follows we fix one such $\mathbf{G}=\mathbf{G}_{\max}$. (In case of point symmetry there are several equivalent ones.)

Now we have a direction $\mathbf{g}$ and a coordinate d in this direction, on the scale of which the positions of the perpendicular sublattice planes are given by a periodic repetition of N coordinates d_s, with $g_s=d_s \bmod 2\pi/|\mathbf{G}|$, with a minimum

spacing $\gamma>0$. [For special directions $\mathbf{g}$ several planes may have the same coordinate d_s; this does not pose problems, if, in the following, pairs (s,s') with $d_s=d_{s'}$ are excluded from consideration.] We define

$$f_s^{(1)}(\mathbf{r}-\mathbf{s})=f(x_{s,s-1}^{(1)})f(x_{s,s+1}^{(1)}),\quad x_{s,s'}^{(1)}=\frac{d-d_s}{d_{s'}-d_s},\quad (71)$$

where $f(x)$ is the function Eq. (36). (Note that the scales for $x_{s,s-1}$ and $x_{s,s+1}$ may be different: $f_s^{(1)}$ need not be symmetric.) The result is obviously a partitioning of unity along the direction $\mathbf{g}$ which is constant perpendicular to that direction. In the following, $\mathbf{g}$ is renamed $\mathbf{g}^{(1)}$.

Our construction ensures that perpendicular to $\mathbf{g}^{(1)}$ we have for each s a two-dimensional lattice with basis. The same construction as above in two dimensions provides a partitioning of unity

$$f_s^{(2)}(\mathbf{r}-\mathbf{s})=f(x_{s,s-1}^{(2)})f(x_{s,s+1}^{(2)}) \quad (72)$$

along a selected direction $\tilde{\mathbf{g}}^{(2)}$ of a two-dimensional reciprocal-lattice vector. Each $\tilde{\mathbf{g}}^{(2)}$ is the projection of a three-dimensional reciprocal-lattice vector, $\mathbf{g}^{(2)}$, onto this plane. In fact, it is only necessary to choose $\mathbf{g}^{(2)}$ and $\mathbf{g}^{(1)}$ to be linearly independent. However, we expect the least anisotropic shape functions to be the construction which has the largest angle between $\mathbf{g}^{(1)}$ and $\mathbf{g}^{(2)}$. Now we have two classes of planes giving for each s a function

$$f_s^{(1)}(\mathbf{r}-\mathbf{s})f_s^{(2)}(\mathbf{r}-\mathbf{s}) \quad (73)$$

which still is constant along the direction $\mathbf{g}^{(1)}\times\mathbf{g}^{(2)}$. This direction just defines the crossing lines of the two classes of planes. For these one-dimensional lattices we chose a direction $\mathbf{g}^{(3)}$ close to $\mathbf{g}^{(1)}\times\mathbf{g}^{(2)}$ and use a partitioning of unity

$$f_s^{(3)}(\mathbf{r}-\mathbf{s})=f(x_{s,s-1}^{(3)})f(x_{s,s+1}^{(3)}). \quad (74)$$

This step completes our task Eq. (66) with the *exact* result

$$f_s(\mathbf{r})=f_s^{(1)}(\mathbf{r})f_s^{(2)}(\mathbf{r})f_s^{(3)}(\mathbf{r}). \quad (75)$$

It remains to define $f(x)$ of Eq. (36).

A very simple smooth solution of Eq. (36) is

$$f_1(x)=\frac{1}{2}(\cos\,\pi x+1),\quad 0\leqslant x\leqslant 1. \quad (76)$$

If a smoother solution is needed, one has at hand an infinite sequence

$$f_n(x)=1-f_1(f_{n-1}(x)),\quad n=2,3,\ldots\ . \quad (77)$$

Suppose that $f_{n-1}(x)+f_{n-1}(1-x)=1$ as in Eq. (36). This immediately implies

$$\begin{aligned} &f_n(x)+f_n(1-x)\\ &\quad=1-f_1(f_{n-1}(x))+1-f_1(f_{n-1}(1-x))\\ &\quad=2-f_1(f_{n-1}(x))-f_1(1-f_{n-1}(x))=1. \end{aligned} \quad (78)$$

Hence, the construction Eq. (77) is not limited to the form of Eq. (76) but is possible with every function Eq. (36).

Following this procedure with open structures, it may happen that, despite the minimax approach to the first step, rather elongated site cells result for certain sites. This is a clear indication of the beneficial introduction of empty sites occupying the remote parts of the elongated cells. If one wants to avoid empty sites, one can try the second best selection in Eq. (70).

A final step is left to be made. For both symmetry reasons as well as the desired minimal anisotropy of $f_s(\mathbf{r})$, one would like to have

$$f_{Us}(\mathbf{r})=f_s(u_0\mathbf{r}), \quad (79)$$

where U is any symmetry transformation of the lattice and u_0 is its point symmetry content. Let M be the order of the point group of the lattice considered and form

$$\overline{f_s}(\mathbf{r})=\frac{1}{M}\sum_{u_0} f_{Us}(u_0^{-1}\mathbf{r}). \quad (80)$$

Obviously, this again provides a partitioning of unity on the given lattice with the wanted symmetry property.

A very important point is that we have not only a smooth partitioning of unity on the lattice, Eq. (66), but one where every f_s has compact support (the domain outside of which $f_s=0$), *which excludes all lattice sites from its interior except the center*, and which approaches zero at the neighboring sites with any wanted power law by simply applying Eq. (77) sufficiently often. The second point is that the symmetrization Eq. (80) may be carried out explicitly by using transformation laws of the scalar products $\mathbf{g}\cdot\mathbf{r}$. Thus for each lattice, we end up with a simple explicit expression of the shape function whose calculation will be fast.

III. NUMERICS

In this section we focus on some numerical technicalities used to implement an efficient code. All local functions are represented numerically on a radial mesh starting at some small nonzero radius. The spacing of successive mesh points can be taken either to follow a logarithmic or a power law. Both work well. In actual calculations the radial functions have to be interpolated. We use the Neville algorithm with degree 9.

Several on-site terms must be calculated. The on-site overlap and Hamiltonian matrix elements and the on-site parts of the total energy expressions involve radial integrations and integrations over the unit sphere of products of two or three spherical harmonics. The latter integration reduces to orthogonality relations of the spherical harmonics or Gaunt coefficients, respectively. The radial integrations are done using Gauss quadrature. The expansion of the net density into spherical harmonics contains integrations of products of three spherical harmonics, which again yields Gaunt coefficients.

The two-site matrix elements in their most complicated form are integrals over products of three radial functions and spherical harmonics. These three-dimensional integrations may be reduced to two-dimensional integrations by using the algebra of the angular momentum operator. This has the advantage first of having to control only two mesh parameters and second, by rearrangement of the formulas, a considerable

reduction of the number of operations needed. The expressions have the form (**R** is the vector pointing from a to b)

$$\int d\mathbf{r} f_l^a(r) Y_{lm}(\mathbf{r}) \sum_{L_1} v_{L_1}(r) Y_{L_1}(\mathbf{r}) f_{l'}^b(|\mathbf{r}-\mathbf{R}|) Y_{l'm'}(\mathbf{r}-\mathbf{R}). \tag{81}$$

Now introduce a rotation u of the coordinate system transforming the vector **R** to the vector $(0,0,R)$ $(R=|\mathbf{R}|)$,

$$u\mathbf{r}=\mathbf{r}', \quad n\mathbf{R}=(0,0,R). \tag{82}$$

Then we may use spherical coordinates r,θ,ϕ or bipolar coordinates ξ,η,ϕ about the axis $(0,0,R)$, where ϕ represents the rotation angle about the axis. (For definition of the bipolar coordinates see standard mathematical textbooks.) The gain is that the argument $r_b=|\mathbf{r}-\mathbf{R}|$ no longer depends on ϕ. The rotation algebra of spherical harmonics gives

$$Y_{lm}(\mathbf{r})=Y_{lm}(u\mathbf{r}')=\sum_{m'} a_{mm'}^l Y_{lm'}(\mathbf{r}'), \tag{83}$$

where $a_{mm'}^l$ are the representation matrix elements. The next step is to write the definition of our (''real'') spherical harmonics

$$Y_{lm}(\theta,\phi)=i^l P_l^{|m|}(\cos\theta) g_m(\phi) \tag{84}$$

with

$$g_m(\phi)=\begin{cases} \sin|m|\phi & \text{for} \quad m=-1,\ldots,-l \\ \cos|m|\phi & \text{for} \quad m=0,\ldots,l. \end{cases} \tag{85}$$

The only ϕ-dependent parts of Eq. (81) are now those of the Y_L. Hence, the ϕ integration may be performed analytically, resulting in the selection rules

$$(m_1 m_2 m_3)=\int g_{m_1}(\phi) g_{m_2}(\phi) g_{m_3}(\phi) d\phi. \tag{86}$$

Now, we rewrite Eq. (81) (using spherical coordinates)

$$i^{l-l'} \sum_{l_1,m_1 m_2 m_3 m_4} \int_0^\infty r^2 dr \int_0^\pi d\cos\theta f_l^a(r) a_{mm_2}^l P_l^{m_2}(\theta) v_{m_1}^{l_1}(r) a_{m_1 m_3}^{l_1} P_{l^1}^{m_3}(\theta) f_{l'}^b(r_b) a_{m'm_4}^l P_{l'}^{m_4}(\theta_b)(m_2 m_3 m_4) \tag{87}$$

with $\theta_b=(r\cos\theta-R)/r_b$ and $r_b^2=r^2+R^2-2rR\cos\theta$. One point offering the possibility to reduce the number of operations is that the radial orbital functions f_l^a do not depend on m. Furthermore, the vectors to the neighboring sites around a may be classified into shells containing vectors $\mathbf{R}+\mathbf{s}$ of the same length, differing only in **R**. The two-dimensional integrals Eq. (87) may be performed in bipolar coordinates as well. They are applicable to all two-center terms and also to the overlap density calculations. In the latter case, one has to multiply by the multicenter partitioning function $f(x)$, which after rotation u does not depend on ϕ either. Then one calculates for a number of radial mesh points the θ integral only, dropping v_{L_1} and collecting the $l_1 m_1$ terms which are the L_1 components of the angular momentum expansion of the overlap density. Finally, the resulting radial functions are reinterpolated on the original radial mesh. This reduction to two-dimensional integrals is always possible, if all radial functions involved do not depend on ϕ after the rotation u. The two remaining integrations are treated by Gaussian quadratures. The number of mesh points is determined by the requirement of a $<10^{-6}$ Hartree accuracy of the Hamiltonian integrals, or a $<10^{-6}$ accuracy of the overlap integrals or density values measured with respect to the normalization.

The integrals in Eq. (49) are performed as Gaussian quadratures too. Now, the remaining integrals are really three-dimensional. First, there are the three-center contributions to the Hamiltonian matrix which are performed in spherical coordinates around the center of the potential using Gaussian quadrature for the radial and the θ part and an equal weight integration for the ϕ coordinate. The angular momentum expansion of the local exchange and correlation potential Eq. (57) as well as the local Ewald potential Eq. (55) involving the shape functions are done in spherical coordinates, too. The same holds for the exchange and correlation energy Eq. (65).

All **k** integrations are performed using the tetrahedron method (cf. Ref. 15).

IV. RESULTS

To illustrate the capability of our method, we report results for a few cases chosen to check various aspects of the concepts developed above. The main focus was on properties such as lattice constant, magnetic moment, and total energy to test the influence of the approximations involved. To compare data from the same spin density functional, all calculations were done nonrelativistically with the LSDA of Perdew and Zunger.[30] This holds also for the data obtained with other methods and given in Tables I–IV for comparison.

TABLE I. Aluminum: total energy E_{tot} (Hartree), lattice constant a_0 (a.u.), and bulk modulus B (Mbar).

	E_{tot}	a_0	B
Present work	-241.461	7.56	0.84
FPLAPW (Ref. 31)	-241.465	7.53	0.86
OPW[a]	$-241.46305 \leqslant E_{\text{tot}} \leqslant -241.46285$		
FPKKR (Ref. 35)		7.55	0.84
Expt.[b]		7.60	0.72

[a]See the text.

[b]All lattice constants (extrapolated to zero temperature) and bulk moduli are taken from Ref. 36.

TABLE II. Aluminum: theoretical 0 K transition pressures (P in GPa) and volumes (V/V_{300}, $V_{300}=112$ a.u.) for the fcc-hcp and hcp-bcc phase transition. The lower experimental bound for the fcc-hcp transition is about 219 GPa.

	fcc-hcp		hcp-bcc	
	P	V/V_{300}	P	V/V_{300}
Present work	200±30	0.51	235±40	0.48
LCGTO-FF (Ref. 33)	205±20	0.51	565±60	0.364
LMTO-ASA (Ref. 37)	120		200	
AP (Ref. 38)	220	0.5	380	0.4

A. Aluminum

We begin with the free-electron-like metal aluminum. As valence orbitals we take $3s3p3d$, where the d orbitals are needed for completeness of the basis and are occupied by a few tens of electrons. In Sec. II A we introduced a confining potential $(r/r_0)^4$, $r_0=(x_0 r_{\mathrm{NN}}/2)^{3/2}$, to tune the local valence orbitals. The choice of x_0 determines the quality of the basis set. Thus one would expect the total energy to be minimized by taking optimal values for these parameters. In Fig. 1 the variation of the total energy with respect to x_0 is shown for a fixed lattice constant and angular momentum cutoff $L_{\max}$. The $3s$ and $3p$ compression parameters are set equal since the extent of these orbitals is comparable. Thus we have two values $x_0(sp)$ and $x_0(d)$. The figure contains two curves representing the total energy change with respect to one x_0 while fixing the other at its optimal value. Indeed, as can be seen, there exist optimal values for both x_0. The variation of the sp parameter within ±5% gives a change in the total energy of about 1 mHartree. The d parameter is less critical because of the small d-wave admixture in the occupied Kohn-Sham states.

The preceding discussion was restricted to a minimum basis choice. Particularly, the subdivision of the orbitals into core and valence orbitals was not yet checked. Applying the condition Eq. (11) we state that there is a rather small overlap of the semicore $2s2p$ orbitals from different sites. Thus to check the influence of the core-valence subdivision on accuracy we performed calculations with a $2s2p3s3p3d$ valence basis. Since they are strongly localized, the semicore states are nearly dispersionless. Moreover, they do not feel much of the confining potential. Thus one would not expect the total energy to be sensitive to the choice of $x_0(2s2p)$. We calculated an energy variation of about 10^{-6} Hartree with respect to the x_0 range shown in Fig. 1. The total energy is raised by 0.07 mHartree with respect to the minimum basis result. There is no reason that the energy is lowered when adding overlapping semicore orbitals to the basis, since the neglect of core-orbital overlap in Eq. (11) introduces an error of indefinite sign. Nevertheless, in the present case this error is far below our accuracy demands, and the treatment of $2s2p$ states as core states is well justified (cf. Fig. 3).

TABLE III. Copper: total energy E_{tot} (Hartree), lattice constant a_0 (a.u.), and bulk modulus B (Mbar).

	E_{tot}	a_0	B
Present work	−1637.932	6.73	1.75
FPLAPW (Ref. 31)	−1637.939	6.73	1.73
LCAO (Ref. 16)		6.71	1.67
FPKKR (Ref. 35)		6.71	1.75
Expt. (Ref. 36)		6.82	1.37

TABLE IV. Diamond: total energy E_{tot} (Hartree), lattice constant a_0 (a.u.), and bulk modulus B (Mbar).

	E_{tot}	a_0	B
Present work	−37.776	6.77	4.3
With empty spheres	−37.794	6.69	4.6
FPLAPW (Ref. 31)	−37.797	6.68	4.7
Expt. (Ref. 36)		6.74	

Having optimized the basis, we come to the second crucial point in our method, namely the potential and density representation. Two approximations are to be checked, the cutoff angular momentum $L_{\max}$ and the steepness of the shape function defined by the number of iterations n used in Eq. (77). In Fig. 2 the dependence of the total energy on both parameters is shown. Two basic conclusions can be drawn. First, the energy converges rather fast with increasing $L_{\max}$. Above $L_{\max}=6$ the energy is almost unvarying for all shape functions with $n>2$. The steepness of the shape function has two competitive effects. The smoother the function is, the faster the angular momentum series converges. On the other hand, the shape function has to fall off sufficiently fast approaching the neighbor atoms. Additionally, it should be unity in as large a region near the nucleus as is possible and its extension over the crystal should be as small as possible. We find that, for $n=1$, which is the most extended function (starting as $1-r^2$ at the nucleus), numerical instabilities are caused. It assigns too much of the potential near the nucleus to neighboring site contributions. From the figure we conclude that $n=3$ seems to be the best choice. (For $n=2$ the screening of the neighbor sites is still not good enough, as may be seen by looking at the functions in real space.) A further increase of the steepness only slows down the L con-

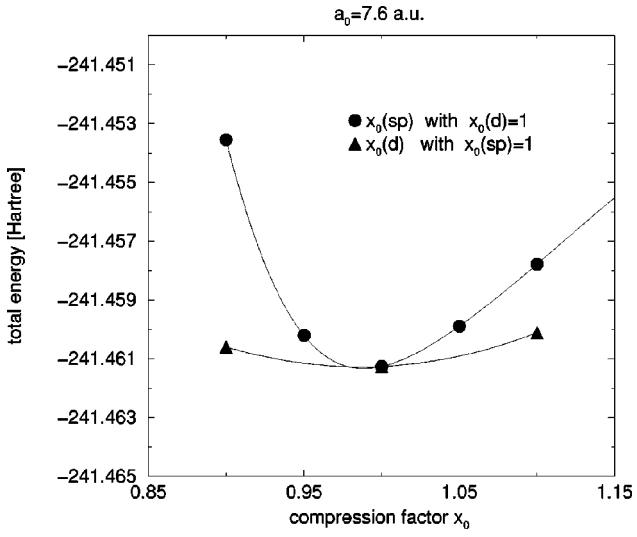

FIG. 1. Variaton of the total energy with respect to the compression parameters for fcc aluminum, $L_{\max}=6$, spd basis.

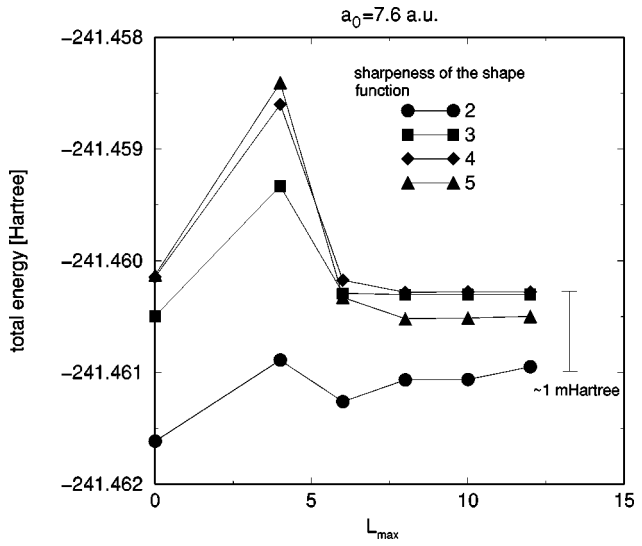

FIG. 2. Dependence of the total energy on the cutoff $L_{\max}$ and the sharpness of the shape function, *spd* basis.

vergence. Finally, we may state that there is an uncertainty of the total energy of about 1 mHartree due to the shape technique.

One remark should be made concerning the convergence of the potential and density with increasing $L_{\max}$. We tested how the total electron density converges with the cutoff momentum and found that already at $L_{\max}>6$ the electron density deviates less than 10^{-5} [electrons/(a.u.)^3] from the $L_{\max}=12$ result. This is due to the fact that the net density has a maximal angular momentum 6 (in the case of *f* orbitals) and that the treatment of the overlap density is rapidly converging with L. In contrast, the shape treatment of the exchange and correlation potential is more sensitive to the cutoff momentum, since the shape function Eq. (80) exhibits the crystal point symmetry and therefore has more features in the higher-order derivations than the quasi-one-dimensional shape function Eq. (38). We compared the total xc potential along various directions calculated directly from the electron density with the result obtained from Eqs. (56) and (57). We found a maximum deviation of 2 mHartree for $L_{\max}=12$. These deviations add up to zero over the whole unit cell, since they originate from the neglect of higher angular momenta, which are orthogonal to the $L=0$ contribution.

In Fig. 3 we show the total energy curve with varying lattice constant. The results for the minimum basis and for the basis with semicore orbitals are presented. Table I summarizes the calculated data in comparison with the results produced by other methods and with experiment. Our lattice constant result deviates from the experimental value by about -0.4%, which is the usual behavior of LSDA calculations. Compared to the FPLAPW (Refs. 31 and 32) results, our total energy lies higher by approximately 4 mHartree/atom. The lattice constant and bulk modulus are nearly the same. Additionally, we performed an orthogonalized plane-wave (OPW) calculation. We tested the convergence of the total energy with respect to the number of OPW's. In Table I the tolerance interval for the energy is given. These bounds hold for more than 2000 OPW's.

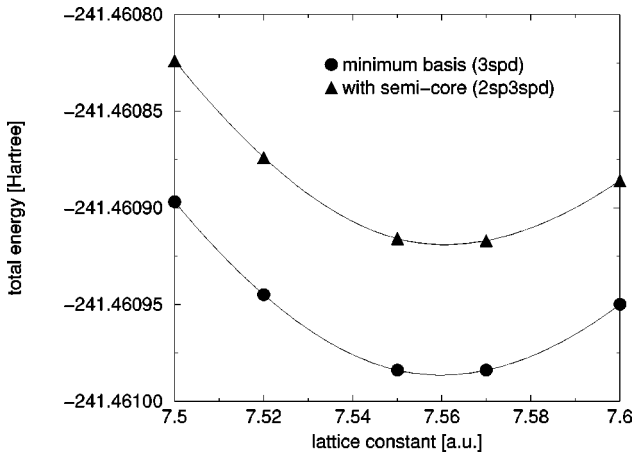

FIG. 3. Total energy versus lattice constant for aluminum with $L_{\max}=12$.

B. Aluminum under pressure

To check the capabilities of our method further, we apply it to aluminum under high pressure. In a recent study of the fcc, hcp, and bcc phase of aluminum,[33] a fcc-hcp phase transition at about 200 GPa and a hcp-bcc transition at about 565 GPa were calculated. To compare with these results we followed the procedure of those authors.

We calculated the total energy at 12 lattice constants between $0.3V_0$ and $1.1V_0$ (V_0 being the equilibrium volume) for all three structures. For each volume we used an optimized set of compression parameters x_0. The changes of the x_0 about this large range of lattice parameters is less than 7%, which results in a maximal energy change of 1 mHartree compared to calculations with fixed x_0. We used about 300 k points in the irreducible Brillouin zone, which gives converged results with respect to the number of k points. As exchange and correlation potential we chose the LSDA version of Perdew and Zunger,[30] that is derived from the best quantum Monte Carlo calculations for the electron gas available at present.

These total energy data were fitted to an equation of state (EOS) of the functional form

$$E(a)=-(E_0+E_1)+E_1\left(1+\frac{a-a_0}{l}\right)\exp\left(-\frac{a-a_0}{l}\right). \tag{88}$$

Here, a_0 is the zero pressure lattice constant, $-E_0$ is the ground-state energy, l is a scaling length, and E_1 is related to the bulk modulus. (The energy zero, of course, is arbitrary in the above equation.) This functional form gives a very good fit to the total energy data. The derivative of the EOS with respect to the volume gives the negative of the pressure. Figure 4 shows the dependence of the pressure on the volume for all three structures compared to experimental data. As can be seen, the curves for the three structures are not very different. This is due to the fact that the total energy curves are very similar. The agreement of the theoretical and the experimental results is quite good. In Ref. 33 a phonon contribution was added to the 0 K results to compare better with the experiments. However, the influence of this correction was small.

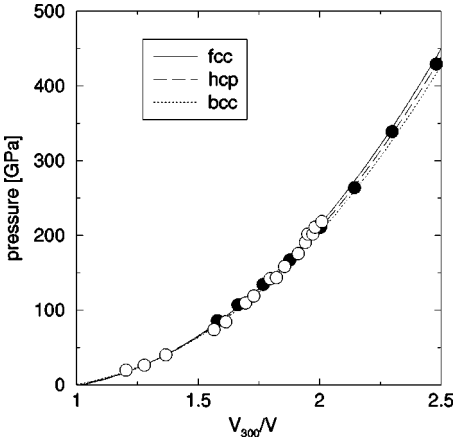

FIG. 4. Pressure versus compression (V_{300}/V, $V_{300}=112$ a.u. being the experimental 300 K equilibrium volume) for aluminum. The lines are the theoretical results for 0 K. The open symbols are room-temperature diamond-anvil-cell measurements (Ref. 34) and the filled symbols are derived from shock data (Ref. 39).

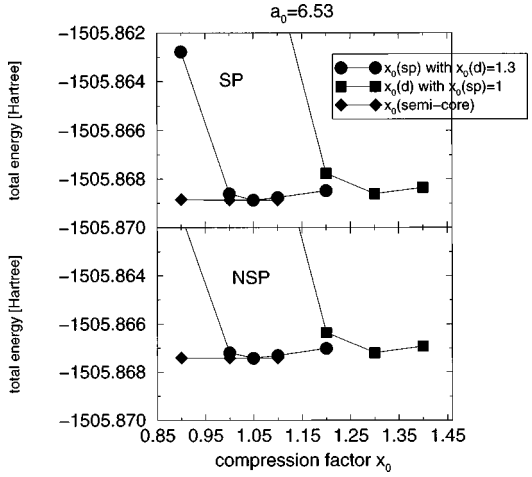

FIG. 5. Total energy versus compression parameter for nickel ($L_{\max}=12$). The spin-polarized (upper panel) and non-spin-polarized (lower panel) calculation.

From the EOS the enthalpy may be calculated. The crossings of the enthalpy curves give the transition pressures for the various phase transitions. Table II gives our results and some data from other calculations. The errors are due to an uncertainty in the total energy of about 1 mRydberg. We only show the physical transitions which are fcc-hcp and hcp-bcc. Our result for the first transition pressure (fcc-hcp) is well within the range of the results given in Table II. The LMTO-ASA value seems to be too small since the measurements in Ref. 34 found a stable fcc structure up to 219 GPa. Thus, our fcc-hcp transition pressure compares well with other calculations and is not in contradiction to the experiment. The second phase transition (hcp-bcc) is predicted by our calculation at a remarkably lower pressure, compared to other methods (except LMTO). Since an experimental justification of this static lattice phase transition is not yet present, we cannot discuss the validity of the results. As a test of our calculation we enlarged the basis set, including the $2s2p$ and $4s$ orbitals into the valence states. But this did not change the results. As far as experimental data being present for aluminum under high pressure, our results compare quite well with them.

C. Transition metals

The next example will be copper. The minimum basis set for copper is given by $4s4p3d$. The semicore states are $3s3p$. Again, we determined the optimal x_0 for the three classes of orbitals $3s3p$ (if treated as valence states), $4s4p$, and $3d$ by energy minimization. The result was $x_0(4s4p)=1.1$ and $x_0(3d)=1.3$. The energy variation while changing the compression parameters by about $\pm 5\%$ is less than 1 mHartree. If we add the semicore orbitals to the valence set, the energy variation with x_0 is of the order 10^{-6} Hartree. The effect of adding these orbitals is a constant energy shift of about 0.5 mHartree. Again the energy is raised. (See the discussion above.) Table III gives the lattice constant and bulk modulus in comparison with other results. The lattice constant and bulk modulus are the same as from FPLAPW results, but our total energy is 7 mHartree/atom too high.

Next, we consider the magnetic elements, starting with nickel. For nickel as well as for iron, the inclusion of the semicore states $3s3p$ into the valence set is unavoidable due to a significant overlap of the orbitals from neighboring sites. So, the minimum basis for this elements is $3s3p4s4p3d$. Still, the bands corresponding to the semicore states are almost dispersionless. The change of the total energy while varying the compression factor of these orbitals by $\pm 20\%$ around the optimum value does not exceed 0.06 mHartree. The remaining parameters for the $4s4p$ and $3d$ states are determined both for spin-polarized and for non-spin-polarized nickel in Fig. 5. It can be seen there that, except for a constant shift, the curves are identical, and the optimum x_0 values are the same: $x_0(sp)=1.05$ and $x_0(d)=1.3$. The shift is the magnetization energy: $E_{\mathrm{mag}}=1.5$ mHartree.

To test the completeness of our basis set, we performed additional calculations using the $4d$ orbital as a supplemental valence orbital. Figure 6 compares the total energy and the magnetization dependence on a single compression factor for both basis sets. The main conclusions are first that the energy variation becomes smaller when adding the $4d$ orbital, and second the magnetic moment becomes almost a constant versus x_0, a clear indication for the onset of basis completeness. Furthermore, the energy is lowered as it should be when variational freedom is increased. Table V summarizes the total energy, lattice constant, bulk modulus, magnetization energy, and magnetic moment (at the theoretical a_0) calculated by different methods.

One point may be stated (see iron below). We find magnetic moments generally smaller than those calculated by MT or ASA approaches but which compare well with other full-potential results. In our view this difference is connected with the treatment of the xc potential. (Compare the discussion about the effect of the linearization of the core xc potential on the magnetic moment in pseudopotential methods.[11]) Thus, one effect of full-potential methods is a reduction of the calculated magnetic moments. This is quite reasonable. The moments determined at the theoretical lattice constant are smaller than those calculated at the experimental a_0. So, μ should be smaller than the experimental value. The trend in MT calculations is to get at least the

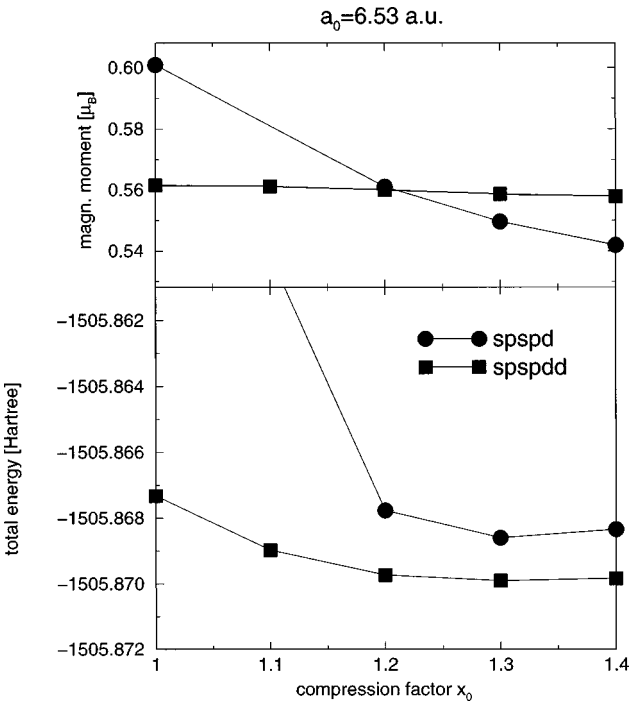

FIG. 6. Total energy (lower panel) and magnetic moment (upper panel) versus $3d$ compression factor for spin-polarized nickel ($L_{\max}=12$) for two different basis sets.

experimental or even higher value for μ. We think that the smaller value given by a number of pseudopotential and full-potential methods is more likely the correct LSDA number.

All the statements above concerning the results for nickel are rather similar for iron. The basis sets and compression factors are the same, and the stabilization of the magnetic moment with switching to the larger basis set (including $4d$ orbitals) takes place the same way. Thus, we refer to Table VI for a summary of our results compared to other calculations and experiment.

D. Diamond

Until now we found rather good results for simple metals and closed-packed structures. However, if the full-potential character of the scheme is to be taken seriously, open structures should be possible to be calculated as well. Surely there are limitations due to the minimum basis, which does not comprise polarization orbitals.

TABLE V. Nickel: total energy E_{tot} (Hartree), magnetization energy E_{mag} (mHartree), lattice constant a_0 (a.u.), bulk modulus B (MBar), and magnetic moment (μ_B),

	E_{tot}	E_{mag}	a_0	B	μ
Present work, *spspd* basis	−1505.869	1.5	6.53	2.41	0.551
Present work, *spspdd* basis	−1505.870	1.5	6.53	2.30	0.559
Pseudopotential (Ref. 11)		1.3	6.50	2.39	0.60
FPLAPW (Ref. 31)	−1505.871		6.53	2.60	0.565
FPKKR (Ref. 35)[a]			6.48	2.53	
Expt. (Ref. 36)			6.65	1.86	0.61

[a]Scalar relativistic calculations.

TABLE VI. Iron: total energy E_{tot} (Hartree), magnetization energy E_{mag} (mHartree), lattice constant a_0 (a.u.), bulk modulus B (Mbar), and magnetic moment (μ_B).

	E_{tot}	E_{mag}	a_0	B	μ
Present work, *spspd* basis	−1261.447	10.0	5.24	2.30	2.04
Present work, *spspdd* basis	−1261.448	10.0	5.24	2.29	2.03
Pseudopotential (Ref. 11)		10.1	5.22	2.26	2.01
FPLAPW (Ref. 31)	−1261.451		5.25	2.26	2.17
FPKKR (Ref. 35)[a]			5.22	2.41	
Expt. (Ref. 36)			5.42	1.68	2.22

[a]Scalar relativistic calculations.

We present our results for diamond, which is a cubic lattice, but has two vacancies along the (111) direction compared to a closed-packed lattice. (If those vacancies were occupied by atoms, the resulting structure would be body centered cubic.) As mentioned in Sec. II F, the construction of the shape function may give a hint where the empty spheres should be placed in the lattice. In the diamond structure the minimax condition Eq. (70) indeed produces cell shapes which are rather compact except along the (111) axis. On this axis the ratio of the distance to the neighboring atoms in opposite directions is 1/3. If we introduce two equally spaced empty spheres on this axis, we arrive at a bcc-like filling of the lattice. Accepting the introduction of empty spheres, one again has the rather isotropic cell shapes produced by the bcc structure. To get more isotropic cell shapes without introducing empty spheres, one has to relax the minimax condition. Then one finds orthogonal cells which are centered around the atoms but still have the edge ratio 1/(2.8)/(2.8). After applying the space-group symmetry, one ends up with centered shape functions having smooth but steplike features.

To test our approach we compared calculations for diamond, both using the shape function described above and using empty spheres. Begin with the direct calculation without empty spheres. As a valence set we took $2s2p3d$. (The effect of treating the $1s$ orbital as a valence state was not examined.) Then we found, via energy minimization, the optimal values, $x_0(sp)=1.3$ and $x_0(d)=1.3$. The maximum energy difference under $\pm 5\%$ variation of the x_0 is 3 mHartree/atom. Testing the convergence of the energy with the cutoff $L_{\max}$ and the shape function interation depth n, we found an uncertainty of about 3–4 mHartree/atom. The calculated lattice constant and bulk modulus are given in Table IV. Our lattice constant is about 1.0% too high.

The calculation for diamond including empty spheres was performed with the $2s2p3d$ basis set for the carbon atoms and with the $1s2p$ basis set for the empty spheres. The latter set should be large enough to ensure sufficient variational freedom at the vacancy positions. The compression parameters are determined as described above [$x_{0,C}(sp)=1.1$, $x_{0,C}(d)=1.0$, $x_{0,\text{em.sp.}}(sp)=1.0$], and the energy change with x_0 is of the same order of magnitude as before. Since the shape functions for this calculation are much more spherical than in the former calculation, one would expect faster convergence of the energy with $L_{\max}$ and n. This is the case and the uncertainty of the energy is about 2 mHartree/atom. Ad-

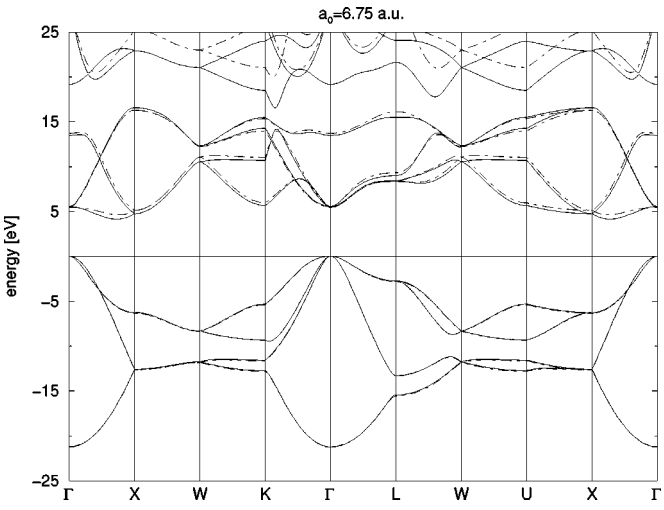

FIG. 7. Diamond: electron bands calculated with empty spheres (full lines) and without empty spheres (dashed lines).

ditionally, the charge density of this calculation is more precise than in the calculation without empty spheres, which leads to a decrease of the total energy by about 17 mHartree/atom. Table IV shows the lattice constant, bulk modulus, and energy. The former two agree now nearly perfectly with FPLAPW results. Thus we can conclude that our method gives rather good results for this open structure even without using empty spheres, and with empty spheres the quality is the same as for close packed structures.

Finally, we present in Fig. 7 the band structure for diamond at $a_0 = 6.75$ a.u. Dashed lines are results without empty spheres while full lines are with empty spheres. For the occupied bands the deviation between both cases is typically 0.05 eV. For the conduction bands both results deviate from one another by up to 1 eV. Clearly, for applications concerning the valence bands only the minimum approach without empty spheres is sufficient.

V. CONCLUSION

We have presented a full-potential band-structure method using only local functions to construct the extended wave functions and the crystal density and potential. The method of linear combination of nonorthogonal overlapping local orbitals has been shown to allow accurate and efficient calculations using a minimum valence basis set. Core relaxation due to the change of the electron density is treated correctly in each self-consistency cycle. The potential was represented as a lattice sum of local nonspherical contributions. It has been verified that with increasing angular momentum cutoff $L_{\max}$ of the L expansion of these local contributions the potential is converging towards the exact crystal potential. This means the scheme presented is full potential.

Calculations on simple structures result in a good agreement with other full-potential methods. The total energy differences between our method and the WIEN95-FPLAPW-code result are a few 10 mHartree/atom. The lattice constants, bulk moduli, and magnetic moments are essentially the same as given by FPLAPW.

The only limitations of our approach are due to the use of a finite basis set (which may be incomplete) and the cutoff momentum $L_{\max}$. However, as has been shown even for open structures such as diamond, the results are quite encouraging. If higher accuracy is needed, the introduction of empty spheres gives a considerable improvement.

An advantage of the present method is the rather low numerical effort. In particular, the dimension of matrices to be diagonalized is kept at the lower limit, which allows one to treat large unit cells. Furthermore, there are some well-established approaches to disordered materials and crystal field calculations and disordered materials based on the main framework used in this scheme, which allows for a direct application of the present method to this problem.

ACKNOWLEDGMENTS

The authors wish to acknowledge P. Novak's assistance in employing the WIEN95 FPLAPW code. We gratefully acknowledge discussions with A. Ernst, whose Ph.D. thesis formed the starting point of the present work. Parts of the code are modifications of the mixed basis code of A. Ernst and H. Eschrig. Finally, we thank J. Forstreuter and M. Richter for their help in clarifying LCAO specific problems.

[1] G. M. Stocks, W. M. Temmerman, and B. L. Gyorffy, Phys. Rev. Lett. **41**, 339 (1978).
[2] A. R. Williams, J. Kübler, and C. D. Gelatt, Jr., Phys. Rev. B **19**, 6094 (1979).
[3] O. K. Andersen, Phys. Rev. B **12**, 3060 (1975).
[4] E. Wimmer, U. Krahauer, K. H. M. Weinert, and A. J. Freeman, Phys. Rev. B **24**, 864 (1981).
[5] P. Blaha, K. Schwarz, P. Sorantin, and S. B. Trickey, Comput. Phys. Commun. **59**, 399 (1990).
[6] B. Drittler, M. Weinert, R. Zeller, and P. H. Dederichs, Solid State Commun. **79**, 31 (1991).
[7] M. Methfessel, C. O. Rodriguez, and O. K. Andersen, Phys. Rev. B **40**, 2009 (1989).
[8] V. Eyert, Ph.D. thesis, Technische Hochschule Darmstadt, 1991.
[9] J. C. Boettger and S. B. Trickey, Phys. Rev. B **29**, 6434 (1984).
[10] J. C. Boettger and S. B. Trickey, Phys. Rev. B **51**, 15 623 (1995).
[11] J.-H. Cho and M. Scheffler, Phys. Rev. B **53**, 10 685 (1996).
[12] A. Zunger and M. L. Cohen, Phys. Rev. B **18**, 5449 (1978).
[13] A. Zunger and M. L. Cohen, Phys. Rev. B **20**, 4082 (1979).
[14] D. Vanderbilt, Phys. Rev. B **41**, 7892 (1990).
[15] H. Eschrig, *Optimized LCAO Method and the Electronic Structure of Extended Systems* (Springer, Berlin, 1989).
[16] G. te Velde and E. J. Baerends, Phys. Rev. B **44**, 7888 (1991).
[17] S. L. Molodtsov, C. Laubschat, M. Richter, Th. Gantz, and A. M. Shikin, Phys. Rev. B **53**, 16 621 (1996).
[18] L. Steinbeck, M. Richter, U. Nitzsche, and H. Eschrig, Phys. Rev. B **53**, 7111 (1996).
[19] J. S. Faulkner and G. M. Stocks, Phys. Rev. B **21**, 3222 (1980).
[20] J. Kudrnovský, V. Drchal, and J. Masek, Phys. Rev. B **35**, 2487 (1987).

[21] R. Zeller *et al.*, Phys. Rev. B **52**, 8807 (1995).
[22] O. K. Andersen and O. Jepsen, Phys. Rev. Lett. **53**, 2571 (1984).
[23] K. Koepernik, B. Velický, R. Hayn, and H. Eschrig, Phys. Rev. B **55**, 5717 (1997).
[24] V. Eyert, K.-H. Höck, S. Fiechter, and H. Tributsch (unpublished).
[25] A. D. Becke, J. Chem. Phys. **88**, 2547 (1988).
[26] N. Stefanou and R. Zeller, J. Phys.: Condens. Matter **3**, 7599 (1991).
[27] J. C. Boettger, Int. J. Quantum Chem., Symp. **27**, 147 (1993).
[28] U. Birkenheuer, J. C. Boettger, and N. Rösch, J. Chem. Phys. **100**, 6826 (1994).
[29] A. Ernst, Ph.D. thesis, Technische Universität Dresden, 1997.
[30] J. P. Perdew and A. Zunger, Phys. Rev. B **23**, 5048 (1981).
[31] P. Blaha, K. Schwarz, P. Dufek, and R. Augustyn, WIN95, Technical University of Vienna, 1995.
[32] P. Novak (private communication).
[33] J. C. Boettger and S. B. Trickey, Phys. Rev. B **53**, 3007 (1996).
[34] R. G. Greene, H. Luo, and A. l. Ruoff, Phys. Rev. Lett. **73**, 2075 (1994).
[35] P. H. Dederichs (private communication).
[36] C. Kittel, *Introduction to Solid State Physics* (John Wiley & Sons, New York, 1986).
[37] A. K. McMahan and J. A. Moriarty, Phys. Rev. B **27**, 3235 (1983).
[38] P. K. Lam and M. L. Cohen, Phys. Rev. B **27**, 5986 (1983).
[39] W. J. Nellis, J. A. Moriarty, A. C. Mitchell, M. Ross, R. G. Dandrea, N. W. Ashcroft, N. C. Holmes, and G. R. Gathers, Phys. Rev. Lett. **60**, 1414 (1988).